Study of junction flows in louvered fin round tube heat exchangers using the dye injection technique

H. Huisseune, C. T'Joen, P. De Jaeger, A. Willockx, M. De Paepe

In: Experimental Thermal and Fluid Science, Vol. 34, pp. 1253-1264, 2010.

Optional: http://dx.doi.org/10.1016/j.expthermflusci.2010.05.006

Study of Junction Flows in Louvered Fin Round Tube Heat Exchangers Using the Dye Injection Technique

H. Huisseune[1,*], C. T'Joen[1], P. De Jaeger[1,2], A. Willockx[1], M. De Paepe[1]

[1]Department of Flow, Heat and Combustion Mechanics, Ghent University,
Sint-Pietersnieuwstraat 41, 9000 Gent, Belgium
[2]NV Bekaert SA, Bekaertstraat 2, 8550 Zwevegem, Belgium
*Corresponding author: Henk.Huisseune@UGent.be; Tel: +3292643289; Fax: +3292643575

Abstract

Detailed studies of junction flows in heat exchangers with an interrupted fin design are rare. However, understanding these flow structures is important for design and optimization purposes, because the thermal hydraulic performance of heat exchangers is strongly related to the flow behaviour. In this study flow visualization experiments were performed in six scaled-up models of a louver fin round tube heat exchanger. The models have three tube rows in a staggered layout and differ only in their fin spacing and louver angle. A water tunnel was designed and built and the flow visualizations were carried out using dye injection. At low Reynolds numbers the streakline follows the tube contours, while at higher Reynolds numbers a horseshoe vortex is developed ahead of the tubes. The two resulting streamwise vortex legs are destroyed by the downstream louvers (i.e. downstream the turnaround louver), especially at higher Reynolds numbers, smaller fin pitches and larger louver angles. Increasing the fin spacing results in a larger and stronger horseshoe vortex. This illustrates that a reduction of the fin spacing results in a dissipation of vortical motion by mechanical blockage and skin friction. Furthermore it was observed that the vortex strength and number of vortices in the second tube row is larger than in the first tube row. This is due to the thicker boundary layer in the second tube row, and the flow deflection, which is typical for louvered fin heat exchangers. Visualizations at the tube-louver junction showed that in the transition part between the angled louver and the flat landing a vortex is present underneath the louver surface which propagates towards the angled louver.

Keywords: heat exchanger; louvered fin; experimental; flow visualization; junction flow; horseshoe vortex

1. Introduction

When exchanging heat with air, the main thermal resistance is located on the airside of the heat exchanger (can contribute up to 85% of the total heat transfer resistance). To improve the heat transfer rate, the heat transfer surface area is increased by adding fins. Tubes can be individually finned (e.g. plain circular fins and helical fins [1-3]) or multiple tubes can pass through each fin. For the latter, which result in a higher compactness, Wang et al. [4] distinguished three generations of fin patterns. The first generation consists of the continuous types, such as plain and wavy fins. When a high compactness is desirable, complex interrupted fin surfaces are preferred. Examples are offset strip fins, slit fins, perforated fins and louvered fins [5]. This second generation of fin designs prevents the formation of thick boundary layers and encourages flow destabilization. The major drawback of the interrupted fin designs is that the associated pressure drop is significant. In contrast to interrupted fin patterns, plain fins with vortex generators enhance the heat transfer rate with relatively low penalty of the pressure drop [6]. Vortex generators provide swirling motion to the flow field which causes an intense mixing of the main flow with the flow in the wall region. They form the third generation of enhanced surfaces.

Figure 1 represents an interrupted section of the louvered fin surface between the tubes. The fin type consists of an array of flat plates (the louvers) set at an angle to the incoming flow. The characteristic parameters of the louvered fin geometry are also indicated in Figure 1. Through a two-dimensional finite-difference analysis, Achaichia and Cowell [7] illustrated that increasing the Reynolds number results in a transition of the flow from duct-directed to more louver-directed. This is an example of ‘boundary layer driven flows’. At low Reynolds numbers the thick boundary layers block the passage between the louvers, forcing the flow to go straight through. As the Reynolds number increases, the boundary layers become thinner and the passage opens up, aligning the flow with the louvers and thus increasing the heat transfer rate. The degree to which the flow follows the louvers is called the flow efficiency. The flow efficiency is strongly dependent on the geometry, especially at low Reynolds numbers [8]. These numerical findings were confirmed by the experiments of DeJong and Jacobi [9], who performed louver-by-louver mass transfer measurements and flow visualizations.

The interrupted section of Figure 1 needs to be connected to the tubes to form the heat exchanger. In modern heat exchangers this is done through a transition of the angled louvers to a flat fin surface (the so called landing), which is then connected to the tubes through mechanical or hydraulic expansion [10]. Cui and Tafti [11] showed that the flow on the angled louver is nominally two-dimensional, which justifies the two-dimensional studies of the flow efficiency discussed above. In the transition region, however, the flow is strongly unsteady and three-dimensional. They performed their calculations for a flat tube surface. In residential air-conditioning and heat pump systems, however, round tubes are commonly used. In this case junction flows are even more complex than in flat tube heat exchangers (used in automotive applications) due to the formation of horseshoe vortices ahead of the tube and wake zones behind. In contrast to the intentionally generated vortices by vortex generators, horseshoe vortices occur naturally in the flow:

adverse pressure gradients around the tube cause the approaching boundary layer to separate, roll up and wrap around the tube [12].

Research on annular finned tubes and plain fin heat exchangers has shown that the fin pitch has a strong impact on the development of horseshoe vortices and thus on the local heat transfer coefficients [2,13-15]. Mon and Gross [2] numerically investigated the flow field and thermal hydraulic behaviour in a four row annular finned tube bundle. They found that the horseshoe vortex system is weak at low Reynolds numbers and for small fin spacings, while it becomes substantial for higher Reynolds numbers and a large fin spacing, resulting in an increased mean heat transfer coefficient. These numerical results are in accordance with the experimental findings of Sung et al. [13], who employed the naphthalene sublimation technique, and Watel et al. [14], who performed infrared thermography and PIV (particle image velocimetry) measurements. Romero-Méndez et al. [15] studied the influence of the fin spacing on the flow field and heat transfer around a cylinder between flat plates, representing a single row plain fin-and-tube heat exchanger. Using flow visualization experiments, they concluded that for small fin spacing no horseshoe vortices are formed upstream of the tube. Horseshoe vortices appear as the fin spacing is increased. Similar results were found for constant fin spacing as the Reynolds number was increased. This study illustrates that reducing the fin spacing can result in a dissipation of vortical motion by mechanical blockage and skin friction. Consequently, the overall heat transfer rate reduces. This direct link between the flow behaviour and the local heat transfer distribution in the tube-fin junction was also investigated by Romero-Méndez et al. [15] by numerical simulations. Romero-Méndez et al. [15] considered a single tube row. Ahrend et al. [16] performed PIV (particle image velocimetry), LDA (laser Doppler anemometry) and AAM (ammonia absorption method) measurements in a three row plain fin heat exchanger and showed that the intensity of the horseshoe vortex system reduces significantly starting from the second row. These findings are not in accordance with the results of Bougeard [17], who performed an infrared thermography investigation of local heat transfer in a plate fin and two-tube rows assembly composed of one fin and circular disks fixed on each side of it. He reported a small horseshoe vortex effect in the first tube row (so only little increase of local heat transfer), while the values of the heat transfer coefficients in front and around the second tube row were higher because the horseshoe vortex was magnified and composed of two vortices. The existence of a multiple vortex structure, which is dependent on the fin spacing and frontal velocity, has also been reported by other authors [13,18,19]. The influence on the local heat transfer rate of the secondary and ternary vortices is smaller than the impact of the primary vortices [13].

Previous studies of horseshoe vortices in heat exchangers were mainly focused on annular finned tubes and plain fin heat exchangers. Detailed studies of horseshoe vortices, and more in general junction flows, in heat exchangers with an interrupted fin design are rare. Hence, the objective of this work is to enlarge the scope of the previous investigations by focusing on the tube-fin junction of louvered fin round tube heat exchangers in which flow deflection and three-dimensional flow in the transition region from the angled louver to the flat landing occur. To this purpose flow visualization experiments were performed on a scaled-up model of a louvered fin heat exchanger with round tubes in a staggered layout. As the louver

angle and fin spacing significantly influence the thermal hydraulic performance of louvered fin heat exchangers [20-22], six enlarged models were tested, which differ only in these two geometrical parameters. As the thermal hydraulic performance of heat exchangers is strongly related to the flow structure, understanding the junction flows is important for design and optimization purposes.

2. Experimental setup and procedure

2.1. Water tunnel setup

A closed loop water tunnel for flow visualization experiments was designed and built, see Figure 2. Water is circulated using a pump with frequency controller (1). It passes through the inlet reservoir (2), the settling chamber (3) and the contraction section (4), before entering the test section (5). The water then flows into the collector (6) from where it is pumped back into the inlet reservoir through a recirculation pipe. A screen with circular holes (7) is placed in the inlet reservoir to make sure that the vortical motions caused by the inlet jet do not propagate to the rest of the water tunnel. A honeycomb flow straightener (cell size ¼ inch - 2 inch long) (8), placed in the settling chamber, breaks the largest vortices and aligns the flow. A mirror, mounted at 45° underneath the test section, allowed for recording bottom view images of the flow through the scaled-up model in the test section. A digital camera was used to record the flow images. Figure 2 also shows the dimensions (in mm) of the water tunnel setup. The test section, with removable lid, has a length of 1000 mm, a width of 440 mm and a height of 270 mm and it is made of transparent plexiglass. Four bent stainless steel plates were welded together forming the contraction section. The walls of the contraction are shaped according to the sinusoidal contours suggested by Byrkin et al. [23] with the inflection point on 1/3 of the contraction length. The contraction length of 1300 mm is determined with the design curves of Rouse and Hassan [24]: long enough to avoid flow separation, but also not too long to avoid too thick exit boundary layers. The contraction ends in a 100 mm long constant area cross section. The area contraction ratio was chosen 6.25:1, so within the range 6-9 recommended by Mehta and Bradshaw [25] to ensure a uniform flow at the inlet of the test section. The cross section of the test section combined with the area contraction ratio determines the cross section of the settling chamber. The settling chamber length was chosen as half of the hydraulic diameter of the settling chamber [26]. The distance between the honeycomb and the contraction entry is ¼ of the hydraulic diameter. The inlet reservoir, settling chamber and collector were manufactured using multiplex plates with a thickness of 18 mm. The resulting uniformity of the velocity profile was verified through laser Doppler anemometry [27]. The results showed that the velocity profile is very flat across the test section.

2.2. Scaled-up models

A scaled-up model (8.3:1) of a louvered fin compact heat exchanger with round tubes was placed in the test section at a distance of 385 mm from the test section inlet. This settling section downstream the contraction was necessary to achieve a steady flow. The heat exchanger tubes were oriented vertically. The scaling factor was selected to obtain sufficient spatial resolution, while keeping the dimensions of the test section

within acceptable limits. DeJong and Jacobi [28] showed that the channel walls can have a profound impact on flow visualization in louvered fin arrays and they presented a calculation method to determine the minimum number of fins required to avoid wall effects. This method was used to guide the selection of the scaling factor. Using the minimum required number of fins results in a flow which is similar to the case of an infinite stack of fins, the so called 'periodic' solution. The number of fins of the tested heat exchanger models was 12, 15 or 18 depending on the fin spacing.

Six scaled-up models of a louvered fin compact heat exchanger were tested. They have a staggered 3-2-3 tube layout. In the second tube row two half-tubes are added to avoid bypass flow (see Figure 3). The geometrical parameters of the unscaled models and the scaled models are listed in Table 1. The six models differ in their fin spacing s (and thus fin pitch F_p) and louver angle θ. The parameter values were selected based on a literature survey. Sahin et al. [19] reported that a fin spacing s/d_{ext} between 0.35 and 0.5 corresponds to a minimum pressure drop and high heat transfer for a plain fin-and-tube heat exchanger. The largest fin pitch studied here is between these limits (F_p = 2.53 mm – s/d_{ext} = 0.36). The database of Wang et al. [10] contains samples with a fin pitch ranging from 1.20 to 1.99 mm for louvered fin heat exchangers similar to the geometry tested in this study. The smallest fin pitch was chosen in this range (F_p = 1.71 mm – s/d_{ext} = 0.24). The fin pitch of the third scale model was set in between the two other scaled-up models (F_p = 2.05 mm – s/d_{ext} = 0.29). The louver angle in actual louvered fin heat exchangers typically lies between 15° and 30° [29]. Here, louver angles of 22° and 28° were selected.

Table 1. Geometrical parameters of the (un)scaled test models

Parameter	Symbol	Unscaled	Scaled
Outer tube diameter	d_{ext} (mm)	6.75	56.00
Fin thickness	t_{fin} (mm)	0.12	1.00
Louver pitch	L_p (mm)	1.5	12.5
Louver angle	θ (°)	22; 28	22; 28
Fin pitch	F_p (mm)	1.71; 2.05; 2.53	14.2; 17.0; 21.0
Transversal tube pitch	X_t (mm)	17.6	146.3
Longitudinal tube pitch	X_l (mm)	13.6	112.9

The geometry of the louver elements between the tubes is shown in Figure 1. Each louver element consists of an inlet and exit louver and two louvers on either side of the turnaround louver. The louvered fins for the models with a louver angle of 22° and the models with a louver angle of 28° were made with different manufacturing techniques. For θ = 22°, the fins and louvers were laser cut in transparent polycarbonate sheets with a thickness of 1 mm. Then the louvers were glued together with the fins. A mold was used to ensure that their positions and angle were correct. A close-up image of the louver-tube junction is shown in Figure 4a. In reality the louver transitions from an angle θ into a flat landing adjoining the tube surface. This transition is due to the manufacturing process of the fins (stamping of thin aluminum sheets with advanced dies). To make the models more realistic, it was decided to thermoform the second series of louvered fins (louver angle θ = 28°). In this manufacturing process a transparent polycarbonate sheet (thickness 1 mm) was heated in an oven to a pliable forming temperature so that it could be stretched into a

mold and cooled to the finished shape of the louvered fin. Figure 4b shows a close-up image of the resulting louver-tube junction with the angled louver, transition part and flat landing. The spanwise dimensions of the flat landing and transition part were chosen as in [11], i.e. $0.25L_p$ for the minimum flat landing (between the turnaround louver and tube) and $0.5L_p$ for the transition part.

Next, the fins and tubes were assembled together. Figure 3 shows how the test model was built up. Rings (outer diameter 56 mm, i.e. d_{ext}) with a height equal to the fin spacing were slid over the tubes (outer diameter 50 mm) ensuring the correct distance between the fins. The tubes and rings are made of plexiglass. The end rings are screwed onto the tubes securing the assembly.

2.3. Experimental procedure

Flow visualization was performed by injecting dye in the test section (indicated as (9) on Figure 2). The density difference between the dye and the surrounding water should be as small as possible to ensure a minimal flow disruption. Considering the resulting image contrast as well as a maximum duration of the tests (the circulating water changed color after a while), a solution of Acid Blue 9 in water was selected. The dye was gravimetrically fed to a 1.2-mm-diameter injection tube. The injection rate was adjusted with a drip valve to match the injection velocity to the water velocity in the test section. Dye was injected approximately 1 cm upstream of the model.

Dissolving 0.075 grams of Acid Blue 9 powder in 0.5 liters of water resulted in a negligible density difference between the dye solution and surrounding water (the densities were measured with an Anton Paar DMA 4100 density meter with an accuracy of 0.1 kg/m³). Thus the Richardson number Ri (Eqs. (1)-(3)), which represents the ratio of the buoyancy forces to viscous forces, is close to zero. This ensures that the dye does not sink to the bottom, even at low Reynolds number flows.

$$\mathrm{Ri} = \frac{Gr_{Lp}}{\mathrm{Re}_{Lp}^2} \tag{1}$$

$$\mathrm{Gr_{Lp}} = \frac{g \cdot L_p^3 \cdot \Delta\rho}{\nu^2 \cdot \rho} \tag{2}$$

$$\mathrm{Re_{Lp}} = \frac{V_c \cdot L_p}{\nu} \tag{3}$$

Visualization was done starting from a Reynolds number $\mathrm{Re_{Lp}}$ of about 190. Up to a Reynolds number $\mathrm{Re_{Lp}}$ of about 1100 a straight dye line could be visualized throughout the test section. Above this Reynolds number unsteady motions became noticeable. The flow visualizations were performed up to a Reynolds number $\mathrm{Re_{Lp}}$ of about 880.

The inlet velocities were determined by measuring the time required for a dye streak to travel a distance of 250 mm (with the scale model placed at the end of the test section). The measurement was repeated ten times and the averaged value was used to determine the velocity. This resulted in water velocities between

1 and 6 cm/s. The uncertainty on the Reynolds numbers was determined according to Moffat [30]. Twice the standard deviation of the time measurements was used as uncertainty on the time measurements. The distance was measured using a ruler and an uncertainty of 0.5 cm was used in the error propagation. The maximum velocities in the scaled-up models were determined using the contraction ratio σ (Eqs. (4) - (5)). An uncertainty of 0.4 mm was assumed for the louver pitch. The water temperature was measured using a thermometer (uncertainty value of 0.2°C). The thermodynamic properties of water were calculated based on the IAPWS IF-97 formulation [31]. The uncertainties on the water density and dynamic viscosity are 0.001% and 1%, respectively [31,32]. The root-sum-square method for error propagation [30] resulted in uncertainties on the Reynolds numbers which were smaller than 6%.

$$\sigma = \frac{\left(s + t_{fin}\right) \cdot X_t}{s \cdot \left(X_t - d_{ext}\right)} \tag{4}$$

$$V_c = \sigma \cdot V_{front} \tag{5}$$

3. Results and discussion

3.1. Flow field through the heat exchanger

Figure 5a-b shows the side view and bottom view of a scaled-up model placed in the test section of the water tunnel. The test section walls as well as the flow direction are indicated. The path followed by a dye streakline through the heat exchanger is dependent on the injection position upstream the scaled-up model. As this study focuses on junction flows, streaklines flowing around a tube in the first, second or third tube row were visualized. Firstly dye was injected upstream the middle tube in the first tube row (solid arrow in Figure 5b). When entering the heat exchanger, the dye accelerates due to the contraction. The streakline wraps around the tube. At low Re_{Lp} the streakline follows the tube contour till an angle of about 110°-130° (measured from the front stagnation point), where it separates from the tube surface. The separation point is dependent on the Reynolds number and fin spacing: an increase in Re_{Lp} or fin spacing results in a decrease of the separation angle. This is consistent with the flow separation on a circular cylinder [33]. At higher Re_{Lp} a horseshoe vortex is formed in front of the tube because the adverse pressure gradients cause the approaching boundary layer to separate and roll up to form a span wise vortex at the leading edge. The vortex is wrapped around the tube, resulting in two streamwise vortex legs. However, these vortex legs are destroyed by the downstream louvers (i.e. downstream the turnaround louver) of the first tube row, especially at higher Re_{Lp}, smaller fin pitches and larger louver angles. In the passage between the tubes the flow accelerates because of the reduced cross section. Next, the dye enters the louver array of the second tube row. At high Reynolds numbers the dye streakline was no longer visible, because of the intense mixing due to unsteady flow. At lower Re_{Lp}, where the dye streakline was still visible, a duct or more louver directed flow was observed depending on the Reynolds number, fin spacing, louver angle and relative position of the streakline in the fin passage. The deflection of the flow in louvered fin designs, quantified with the flow efficiency, and the influencing parameters have already been extensively

investigated in the past (e.g. Zhang and Tafti [8], DeJong and Jacobi [9]). As the findings in the current flow visualization study were similar to previous published results, the flow deflection will not be discussed further here. Next, the flow enters the third tube row. The flow follows the path of least resistance: the streakline rolls up forming a horseshoe vortex in front of the tube and then wraps around the tube or it is deflected towards the louver array in the third tube row. Both flow paths are illustrated in Figure 6. The path of least resistance is determined by the relative position in the fin passage where the streakline enters the third tube row. This position (close to the fin surface or more in the center of the fin passage) is in turn determined by the degree of flow deflection at the exit of the second tube row. Finally, the streakline leaves the heat exchanger. Figure 6a also shows that for a streakline close to the fin surface, the dye colors the wake zone behind the tube (in the case of Figure 6a the tube in the first tube row). This was not observed for a streakline at some distance of the fin surface (see Figure 6b). This suggests that the dye streakline is forced towards the wake zone by the louvers. The same flow effect was also observed in the heat exchanger models with $\theta = 28°$, as illustrated in Figure 7a. Two recirculation bubbles are clearly visible. Here flow was injected 1 cm upstream the heat exchanger model in front of the louver array (dashed arrow in Figure 5b). The dye streakline enters the scaled-up model, accelerates and deflects. The degree of flow deflection is again dependent on the relative injection position over the fin passage, the geometry and the Reynolds number. In front of the middle tube in the second tube row a horseshoe vortex (or even multiple vortices as will be shown further on) is developed which wraps around the tube. Depending on the relative position of the dye streakline in the fin passage the recirculation region is filled with the dye or the vortex legs move around the tube without being destructed by the louvers or wake. The streakline exits the heat exchanger via the louver array in the third tube row (see Figure 7b).

3.2. Flow in the vicinity of the tube-louver junction

As discussed previously, in actual louvered fin heat exchangers the angled louver transitions to a flat landing. In the scaled-up models with louver angle of 28° this transition part is present. This section focuses on the flow at the tube-louver junction. Cui and Tafti [11] performed numerical simulations in a louver geometry and showed that the flow in the transition region is strongly three-dimensional. They found that the louver top surface experiences large velocities due to the reduction of the flow area between two adjacent louvers as the louvers approach the flat landing and that underneath the louver a vortex jet is formed. Figure 8 shows a flow image in the tube-louver junction of the second tube row for $Re_{Lp} = 489$, $s/L_p = 1.60$ and $\theta = 28°$. The injection point over the fin passage was chosen such that the dye streakline exiting the louver bank of the first tube row deflects towards the junction of the louver bank of the second tube row (in other words, the dye streakline did not roll up forming a horseshoe vortex). Figure 8a, a side-view flow image of the second tube row, reveals that the dye streakline splits up over the louvers upstream the turnaround louver. Zooming in on the inlet louver (see Figure 8b) shows that a vortex is present in the transition part underneath the louver surface. This vortex propagates towards the angled louver and then moves away from the louver surface to the downstream direction. This is in accordance with the numerical

findings of Cui and Tafti [11]. The flow acceleration over the louver top surface near the junction was also observed during the flow visualizations.

3.3. Horseshoe vortex system

Dye was injected in the test section to visualize horseshoe vortices in front of the tubes in the three tube rows. The flow visualizations were performed in the center of the model. As in the current research the fins are interrupted and at least 12 fins are used in the scaled-up models to avoid wall effects, top view images suffer from extensive parallax effect. That is why mainly side view images are reported (the camera positions are indicated in Figure 5b).

3.3.1. First tube row

The solid arrow in Figure 5b shows the dye injection position for vortex visualizations in the first tube row. The flow images are presented in Figure 9 for the three fin spacings and $\theta = 28°$. The reported Reynolds numbers are the mean values of the Reynolds numbers of the different flow images (which were within each other's uncertainty interval). Dye was injected one millimeter below the middle fin. For all Reynolds numbers, the dye streakline did not impact on the tube, but remained at some distance forming a saddle point, as described by Sahin et al. [19]. For the smallest Reynolds number ($Re_{Lp} = 220$) no horseshoe vortex was formed. As the Reynolds number was increased, a three-dimensional horseshoe vortex was developed which wrapped around the tube. At higher Reynolds numbers the vortex rotates more than once around its axis, which shows that the horseshoe vortex became stronger with increasing Reynolds numbers. Besides the Reynolds number, the vortex strength is also dependent on the fin spacing. For instance, at $Re_{Lp} = 286$ a weak horseshoe vortex was formed in front of the tube for $s/L_p = 1.60$, while for the two other fin spacings the vortex was only detected at $Re_{Lp} = 341$ (for $s/L_p = 1.28$) and at $Re_{Lp} = 381$ (for $s/L_p = 1.06$). Thus, at the same Reynolds number, the horseshoe vortex is larger and stronger for the largest fin spacing. This agrees well with the findings of Mon and Gross [2], who reported that the boundary layer development on the tube and fin surface depends on the fin spacing and, hence, a reduction of the fin spacing results in a dissipation of vortical motion by mechanical blockage and skin friction. Similar flow behaviour was found in the scaled-up models with a louver angle $\theta = 22°$. Wang et al. [4] performed flow visualizations in a plain fin staggered configuration with a large fin spacing ($s/d_{ext} = 0.50$) for three different Reynolds numbers (Re_{Wang} = 500, 1500 and 2500; based on the hydraulic diameter). In all cases a horseshoe vortex was observed in front of the tube. Recalculating these three Reynolds numbers to our configuration with the largest fin spacing ($s/d_{ext} = 0.36$) yields to Re_{Lp} = 191, 572 and 954. In contrast to the observations of Wang et al. [4], no vortex was seen at $Re_{Lp} = 191$. However, this may be explained by the smaller fin spacing compared to the fin spacing used by Wang et al. [4]. Also in the water tunnel of Wang et al. [4] the height of the test section is equal to the fin spacing (in other words the top and bottom test section walls serve as the plain fins). Because there is no fin leading edge the boundary layer upstream the tube is thick and hence the horseshoe vortex develops at lower Re_{Lp}. This is consistent with the leading edge effect explained by Kim

and Song [34], who showed that the distance between the leading edge of the fin and the tube row has a major impact on the vortex development: if the distance is too short the vortex development is not significant because the boundary layer is thin.

The vortex system over de tube height was also visualized by injecting dye on four different positions. The dye injection positions are illustrated in Figure 5c and the visualization results are shown in Figure 10 (s/L_p = 1.60, θ = 22°). The three Reynolds numbers are chosen high enough to be sure that horseshoe vortices are formed in the tube-fin junctions (positions 1 and 4). The visualization results show that the horseshoe vortex formed under the fin (position 1) is stronger than the horseshoe vortex formed above the fin (position 4) at the same Re_{Lp}. This suggests that the adverse pressure gradients, which cause the development of the horseshoe vortex, are not the same on both positions. The images taken when the dye is injected from position 3 reveal the formation of a weak secondary vortex, which is rotating in the opposite direction as the primary (main) horseshoe vortex in position 4. As it was not located in the vicinity of the tube-fin junction, this vortex was induced by the primary vortex. Its vortex strength increases with increasing Reynolds number. Images obtained when injecting the dye from position 2 revealed a less prominent secondary vortex, as only at the highest Reynolds number a weak “three dimensional effect” was observed. These induced vortices were also observed for smaller fin spacings, but they were more suppressed.

3.3.2. Second and third tube row

The dashed arrow in Figure 5b shows the dye injection position for vortex visualizations in the second tube row. By varying the injection position, the flow over the fin passage upstream the tube of the second tube row was visualized through a combination of the different images (see Figure 11). The flow images are presented in Figure 12 for s/L_p = 1.60, θ = 22° and Re_{Lp} = 205. Streakline 6 flows both up and down the face of the tube and then passes around the bases of the tube. No vortex was observed. The streakline does not flow parallel with the fin, but is slightly deflected, which is in accordance with the boundary layer driven flow behaviour in louvered fin heat exchangers [8]. Streakline 5, which is closer to the upper fin, flows up the face of the tube, then along the fin away from the tube and into a small vortex rotating in the counterclockwise direction. As the streakline moves still closer to the fin (streakline 4), the dye flows into a large vortex rotating in the clockwise direction. This primary vortex (also called the main horseshoe vortex) is situated between the small counter-rotating vortex and the tube. As the movement of the streakline continues towards the fin the dye flows into an upstream vortex with the same rotation direction as the primary vortex (see streaklines 2 and 1). This vortex is called a secondary horseshoe vortex. The saddle points of the primary and secondary vortex can be clearly seen in a top view image (Figure 13). For higher Reynolds numbers the vortices are stronger and then the small counter-rotating vortex between the primary and secondary vortex becomes more apparent, as is shown in Figure 14a for Re_{Lp} = 284. When moving the streakline towards the bottom fin (streaklines 7 and 8) a similar vortex system was detected, even though it seems less strong than the vortex system in the tube-fin junction underneath a fin. Streakline 8 in Figure 12

reveals a weak secondary vortex. This vortex becomes clearer in Figure 14b at a higher Reynolds number (Re_{Lp} = 373). Similary observations were reported by Baker [35], who performed smoke visualizations around a cylinder mounted on a flat plate. Baker [35] showed that the number of vortices that are formed in the tube-fin junction is dependent on the Reynolds number and the boundary-layer displacement thickness. While in the first tube row no horseshoe vortices were formed at Re_{Lp} = 205, in the second tube row multiple vortices were detected. Thus at the same Reynolds number the vortex strength and the number of vortices is higher in the second tube row than in the first tube row. This is due to the difference in boundary layer thickness. The distance between the leading edge of the fin and the tube in the first tube row (indicated as α in Figure 15a) is shorter than the distance between the exit louver in the first tube row and the tube in the second tube row (β in Figure 15a). Thus the boundary layer in the second tube row is thicker and hence the vortex system larger and stronger. This is consistent with the measurements of Bougeard [17] who performed an infrared thermography investigation of the local heat transfer coefficients in a plate fin and tube assembly. He reported a small horseshoe vortex effect in the first tube row (small increase of local heat transfer), whereas in front and around the second tube the heat transfer coefficient values were higher due to the occurrence of two horseshoe vortices. In contrast, the measurements of Ahrend et al. [16] in a three row plain fin heat exchanger showed that the intensity of the horseshoe vortex system reduces significantly starting from the second row. However, this is because they used the top and bottom walls of the test section as fins and thus a thick boundary layer was present upstream the tubes of the first tube row, which is not the case in an actual plain fin heat exchanger due to the fin leading edge.

Nevertheless it is remarkable that the difference in vortex number and strength between the first and second tube row is so significant for the tested louvered fin heat exchangers. As is shown in Figure 15, for the plain fin designs β' is much larger than α'. Consequently, as the boundary layer thickness grows with the distance from the fin leading edge, the boundary layer in the second tube row is thicker than in the first tube row, which explains the stronger horseshoe vortex system in the second tube row. However, for the tested louvered fin heat exchangers α does not differ a lot from β (see Figure 15) and thus one expects that the boundary layer upstream the tubes in both tube rows is of similar thickness. This suggests that there is another factor which influences the vortex development in louvered fin heat exchangers. Compared to the plain fin designs, in the louvered fin heat exchangers the flow entering the second tube row is more deflected (especially at higher Re_{Lp}) due to the interrupted fin surface. This flow deflection, quantified by the flow efficiency, affects the local pressure distribution and thus the vortex strength of the horseshoe vortex system in the second tube row. T'Joen et al. [36] already showed that in inclined louvered fins the flow deflection influences the local boundary layer thickness. Further research is necessary to study in depth the influence of the flow deflection on the horseshoe vortex development in louvered fin heat exchangers. The existence of a strong vortex system in the second tube row is important for design and optimization purposes.

In contrast to the observations in the first tube row, induced vortices on the tube wall were not observed in the second tube row.

In Figure 16 the horseshoe vortices for three fin spacings are shown ($\theta = 22°$). The flow images for s/L_p = 1.60 and 1.28 are very similar, while for s/L_p = 1.06 the development of the horseshoe vortex is much more suppressed. This is caused by the dissipation of vortical motion due to the small fin spacing.
Horseshoe vortices in front of the middle tube of the third tube row were also observed. However, because the dye was injected upstream the scaled-up model and thus traveled a long distance through the model before entering the third tube row and because unsteady flow patterns already appeared in the third tube row at low Reynolds numbers, it was very difficult to record images with sufficient contrast. Figure 17 shows flow images for the largest fin spacing s/L_p = 1.60 and Re_{Lp} = 279 and 440. The observations were similar to the ones in the other tube rows: an increase in Reynolds number and fin spacing resulted in stronger vortices.

4. Conclusions

In this study flow visualization experiments were performed in six scaled-up models of a louver fin round tube heat exchanger. The models have three tube rows in a staggered layout and differ only in their fin spacing and louver angle. A water tunnel was designed and built and a dye injection technique was used to visualize the junction flows. It was found that at low Reynolds numbers the streakline follows the tube contours, while at higher Reynolds numbers a horseshoe vortex is developed ahead of the tubes. The two resulting streamwise vortex legs are destroyed by the downstream louvers (i.e. downstream the turnaround louver), especially at higher Re_{Lp}, smaller fin pitches and larger louver angles. Besides the Reynolds number, the fin spacing also influences the horseshoe vortex development: increasing the fin spacing results in a larger and stronger horseshoe vortex. This illustrates that a reduction of the fin spacing results in a dissipation of vortical motion by mechanical blockage and skin friction. Furthermore it was observed that the vortex strength and the number of vortices in the second tube row are larger than in the first tube row. Partially this is due to the thicker boundary layer in the second tube row, but it is believed that also the flow deflection, which is typical for louvered fin heat exchangers, affects the vortex development. Visualizations at the tube-louver junction showed that in the transition part between the angled louver and the flat landing underneath the louver surface a vortex is present which propagates towards the angled louver. The results of this study are important for design and optimization purposes, because the flow structures are related to the thermal hydraulic performance of the heat exchanger.

Nomenclature

d	tube diameter [mm]
F_p	fin pitch [mm]
g	gravimetric constant [m/s²]
Gr_{Lp}	Grashof number based on the louver pitch (Eq. (2)) [-]
L_p	louver pitch [mm]
Re_{Lp}	Reynolds number based on the louver pitch and the velocity in the minimum cross sectional area (Eq. (3)) [-]

Ri	Richardson number (Eq. (1)) [-]
s	fin spacing [mm]
t	thickness [mm]
V	velocity [m/s]
X_l	longitudinal tube pitch [mm]
X_t	transversal tube pitch [mm]

Greek symbols

ν	kinematic viscosity [m^2/s]
θ	louver angle [°]
ρ	density [kg/m^3]
σ	contraction ratio (Eq. (4)) [-]

Subscripts

c	minimum cross sectional area
ext	external

Acknowledgements

The authors would like to express gratitude to the FWO (Flemish Fund for Scientific Research) for the financial support (grant no. FWO09/ASP_H/172). The dedication of technician Robert Gillis is well appreciated.

References

[1] R.L. Webb, Air-side Heat Transfer in Finned Tube Heat Exchangers, Heat Transfer Engineering 1(3) (1980) 33-49.

[2] M.S. Mon, U. Gross, Numerical study of fin-spacing effects in annular-finned tube heat exchangers, International Journal of Heat and Mass Transfer 47 (2004) 1953–1964.

[3] H. Huisseune, C. T'Joen, P. Brodeoux, S. Debaets, M. De Paepe, Thermal Hydraulic Study of a Single Row Heat Exchanger With Helically Finned Tubes, Journal of Heat Transfer 132 (2010) in press.

[4] C.C. Wang, J. Lo, Y.T. Lin, C.S. Wei, Flow visualization of annular and delta winlet vortex generators in fin-and-tube heat exchanger application, International Journal of Heat and Mass Transfer 45 (2002) 3803–3815.

[5] R.K. Shah, D.P. Sekulic, Fundamentals of Heat Exchanger Design, John Wiley & Sons, Inc., Hoboken, New Jersey, 2003.

[6] A.M. Jacobi, R.K. Shah, Heat transfer surface enhancement through the use of longitudinal vortices: A review of recent progress, Experimental Thermal and Fluid Science 11(3) (1995) 295-309.

[7] A. Achaichia, T.A. Cowell, Heat Transfer and Pressure Drop Characteristics of Flat Tube and Louvered Plate Fin Surfaces, Experimental Thermal and Fluid Science 1 (1988) 147-157.

[8] X. Zhang, D.K. Tafti, Flow efficiency in multi-louvered fins, International Journal of Heat and Mass Transfer 46 (2003) 1737–1750.
[9] N.C. DeJong, A.M. Jacobi, Localized flow and heat transfer interactions in louvered fin arrays, International Journal of Heat and Mass Transfer 46 (2003) 443–455.
[10] C.C. Wang, C.J. Lee, C.T. Chang, S.P. Lin, Heat transfer and friction correlation for compact louvered fin-and-tube heat exchangers, International Journal of Heat and Mass Transfer 42(11) (1999) 1945-1956.
[11] J. Cui, D.K. Tafti, Computations of flow and heat transfer in a three-dimensional multilouvered fin geometry, International Journal of Heat and Mass Transfer 45(25) (2002) 5007-5023.
[12] R.L. Simpson, Junction Flows, Annual Review of Fluid Mechanics 33 (2001) 415-443.
[13] H.J. Sung, J.S. Yang, T.S. Park, Local convective mass transfer on circular cylinder with transverse annular fins in crossflow, International Journal of Heat and Mass Transfer 39(5) (1995) 1093-1101.
[14] B. Watel, S. Harmand, B. Desmet, Influence of flow velocity and fin spacing on the forced convective heat transfer from an annular-finned tube, JSME International Journal Series B 42(1) (1999) 56-64.
[15] R. Romero-Méndez, M. Sen, K.T. Yang, R. McClain, Effect of fin spacing on convection in a plate fin and tube heat exchanger, International Journal of Heat and Mass Transfer 43(1) (2000) 39-51.
[16] U. Ahrend, M. Buchholz, R. Schmidt, J. Köhler, Investigation of the relation between turbulent fluid flow and local heat transfer in fin-and-tube heat exchangers, Proceedings of the 13th International Heat Transfer Conference, Sydney, Australia, 2006.
[17] D. Bougeard, Infrared thermography investigation of local heat transfer in a plate fin and two-tube rows assembly, International Journal of Heat and Fluid Flow 28(5) (2007) 988-1002.
[18] J.Y. Kim, T.H. Song, Microscopic phenomena and macroscopic evaluation of heat transfer from plate fins/circular tube assembly using naphthalene sublimation technique, International Journal of Heat and Mass Transfer 45(16) (2002) 3397-3404.
[19] B. Sahin, N.A. Ozturk, C. Gurlek, Horseshoe vortex studies in the passage of a model plate-fin-and-tube heat exchanger, International Journal of Heat and Fluid Flow 29 (2008) 340–351.
[20] G. Lozza, U. Merlo, An experimental investigation of heat transfer and friction losses of interrupted and wavy fins for fin-and-tube heat exchangers, International Journal of Refrigeration-Revue Internationale Du Froid 24(5) (2001) 409-416.
[21] Z.G. Qi, J.P. Chen, J. Chen, Parametric study on the performance of a heat exchanger with corrugated louvered fins, Applied Thermal Engineering 27(2-3) (2007) 539-544.
[22] J. Dong, J. Chen, Z. Chen, W. Zhang, Y. Zhou, Heat Transfer and Pressure Drop Correlations for the Multi-Louvered Fin Compact Heat Exchangers, Energy Convers. Management 48(5) (2007) 1506-1515.
[23] A.P. Byrkin, S.P. Ponomaryov, V.S. Ponomaryova, A.P. Filatov, Aerodynamic Design of Nozzles for Subsonic and Transonic Wind Tunnels, proceedings of AGARD conference, Aerodynamics of wind tunnel circuits and their components, Moscow, Russia, 1996.
[24] H. Rouse, M.M. Hassan, Cavitation-Free Inlets and Contractions, Mechanical Engineering 71 (1949) 213-216.

[25] R.D. Mehta, P. Bradshaw, Design rules for small low speed wind tunnels, Technical Notes, Aeronautical Journal of the Royal Aeronautical Society (1979) 443-449.
[26] O.A. León Patiño, Optimization of heat sinks by computational flow dynamics techniques, PhD dissertation, Ghent University, Belgium, 2003.
[27] N. Denys, D. Deserranno, Stromingsonderzoek met Laser-Doppler Anemometrie in een vloeistoftunnel, master thesis (in Dutch), Ghent University, Belgium, 2000.
[28] N.C. DeJong, A.M. Jacobi, Flow, heat transfer, and pressure drop in the near-wall region of louvered-fin arrays, Experimental Thermal and Fluid Science 27 (2003) 237–250.
[29] N.H. Kim, J.P. Cho, Air-side performance of louver-finned flat aluminum heat exchangers at a low velocity region, International Journal of Heat and Mass Transfer 44(9) (2008) 1127-1139.
[30] R.J. Moffat, Describing the uncertainties in experimental results, Experimental Thermal and Fluid Science 1 (1988) 3-17.
[31] Revised release on the IAPWS industrial formulation 1997 for the thermodynamic properties of water and steam (IAPWS-IF97), 2007.
[32] IAPWS Release on the IAPWS Formulation 1995 for the Thermodynamic Properties of Ordinary Water Substance for General and Scientific Use (IAPWS-95), 1996.
[33] H. Schlichting, K. Gersten, Boundary Layer Theory, Springer, Berlin, Germany, 2003.
[34] J.Y. Kim, T.H. Song, Effect of tube alignment on the heat/mass transfer from a plate fin and two-tube assembly: naphthalene sublimation results, International Journal of Heat and Mass Transfer 46(16) (2003) 3051-3059.
[35] C.J. Baker, The laminar horseshoe vortex, Journal of Fluid Mechanics 95(2) (1979) 347-367.
[36] C. T'Joen, H. Huisseune, H. Canière, H.J. Steeman, A. Willockx, M. De Paepe, Interaction between mean flow and thermo-hydraulic behaviour in inclined louvered fins, International Journal of Heat and Mass Transfer, under review.

Figure captions

Figure 1. Louver array with geometrical parameters

Figure 2. Water tunnel setup used for the flow visualization experiments: the different components are numbered and the dimensions are indicated (in mm)

Figure 3. Assembly of tubes, fins and rings. The rings, with height equal to the fin spacing, ensure the correct distance between the fins

Figure 4. A close-up image of the louver array between two tubes. (a) the angled louvers are glued to the fin; (b) angled louvers are connected with the fin via a transition part using thermoforming

Figure 5. Dye injection positions upstream the scaled-up heat exchanger in the test section: (a) side view; (b) bottom view; (c) dye injection positions for vortex visualization over the tube height. The cameras show the angle under which side view images of the horseshoe vortices were recorded.

Figure 6. Streakline through the staggered tube layout for two different injection positions over the fin passage (Re_{Lp} = 193, s/L_p = 1.28 and θ = 22°) in front of the middle tube of the first tube row. (a) the dye colors the wake zone behind the tube and a horseshoe vortex is present in front of the tube of the third tube row; (b) the wake zone is not colored and no horseshoe vortex is seen in the third tube row because the streakline is further away from the fin surface.

Figure 7. Streakline through the staggered tube layout for two different injection positions over the fin passage. (a) a horseshoe vortex is formed in front of the tube in the second tube row and two recirculation bubble are clearly visible downstream the tube (s/L_p = 1.06; θ = 28° and Re_{Lp} = 284); (b) a horseshoe vortex is visible in front of the tube and the vortex leg wraps around the tube without being destroyed by the louvers or wake (s/L_p = 1.28; θ = 22° and Re_{Lp} = 368).

Figure 8. Side-view flow image of the flow in the junction of the louver array of the second tube row (s/L_p = 1.60, θ = 28° and Re_{Lp} = 489). (a) The dye streakline splits up over the upstream louvers; (b) close-up image of the dashed rectangular in figure (a) showing the vortex formed underneath the inlet louver.

Figure 9. Horseshoe vortex in front of the middle tube of the first tube row for θ = 28°, different Reynolds numbers Re_{Lp} and the three fin spacings (flow direction from left to right)

Figure 10. Primary and secondary vortices over the tube height in front of the middle tube of the first tube row for s/L_p = 1.60 and θ = 22° (flow direction from left to right)

Figure 11. Streaklines approaching the second tube row: by moving the dye injection tube vertically, it was possible to visualize the flow on eight different positions upstream the tube of the second tube row.

Figure 12. Vortices in front of the tube in the second tube row for s/L_p = 1.60, θ = 22° and Re_{Lp} = 205. The flow images are numbered in accordance with the streakline numbers of Figure 11.

Figure 13. Saddle points S_1 and S_2 in front of the tube of the second tube row (s/L_p = 1.60; θ = 22°; Re_{Lp} = 205)

Figure 14. (a) counter-rotating vortex formed in front of the tube in the second tube row (Re_{Lp} = 284); (b) secondary vortex with the same rotation direction as the primary vortex developed upstream above the fin surface for Re_{Lp} = 373 (s/L_p = 1.60; θ = 22°)

Figure 15. Plain fin surface for boundary layer development upstream the tube in the first tube row (α) and upstream the tube in the second tube row (β): (a) louvered fin heat exchanger and (b) plain fin heat exchanger

Figure 16. Horseshoe vortex in front of the tube in the second tube row ($\theta = 22°$)

Figure 17. Horseshoe vortex formed in front of the tube of the third tube row ($s/L_p = 1.60$ and $\theta = 22°$): (a) $Re_{Lp} = 279$; (b) $Re_{Lp} = 440$

List of figures

Figure 1

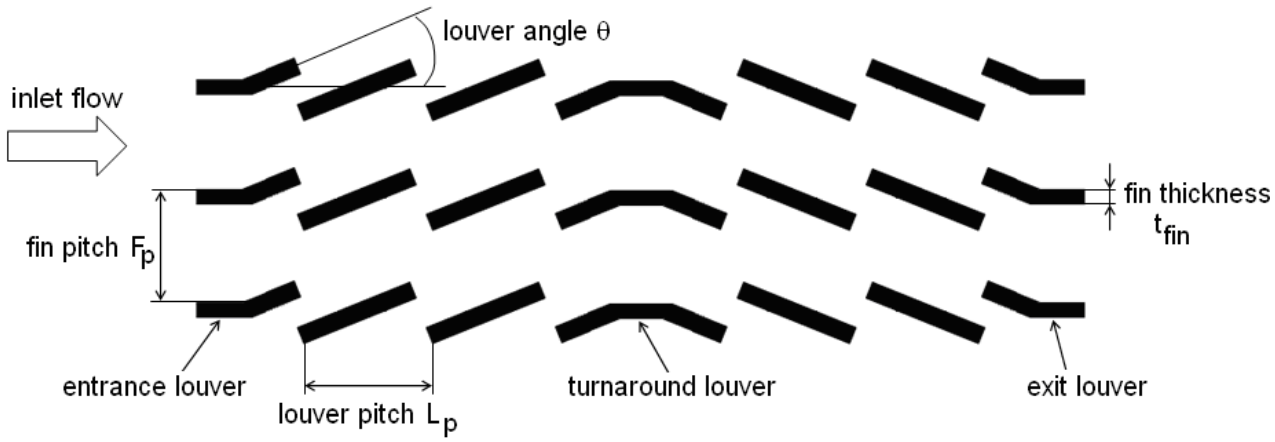

Figure 2

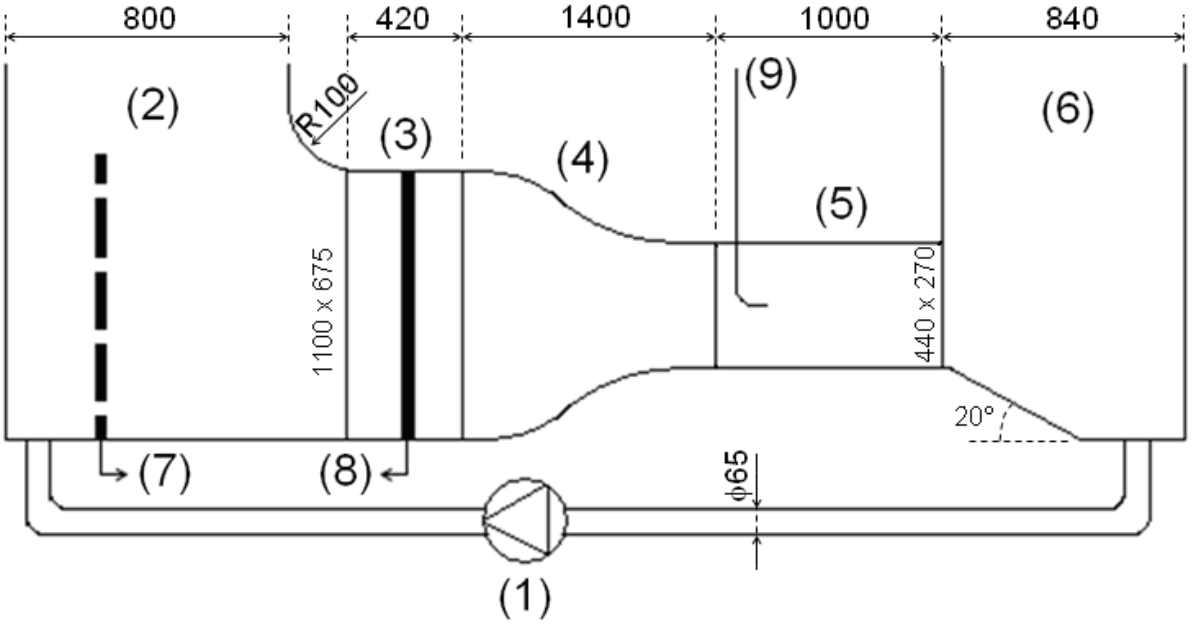
800
420
1400
1000
840
(2)
R100
(3)
(4)
(5)
(9)
(6)
1100 x 675
440 x 270
20°
(7)
(8)
ϕ65
(1)

Figure 3

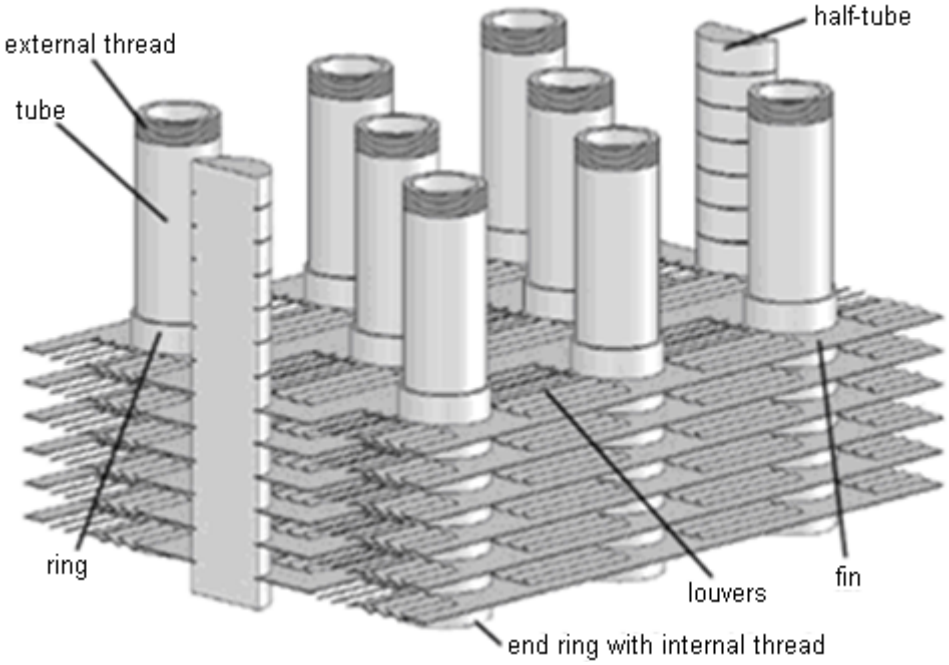
external thread
tube
half-tube
ring
louvers
fin
end ring with internal thread

Figure 4

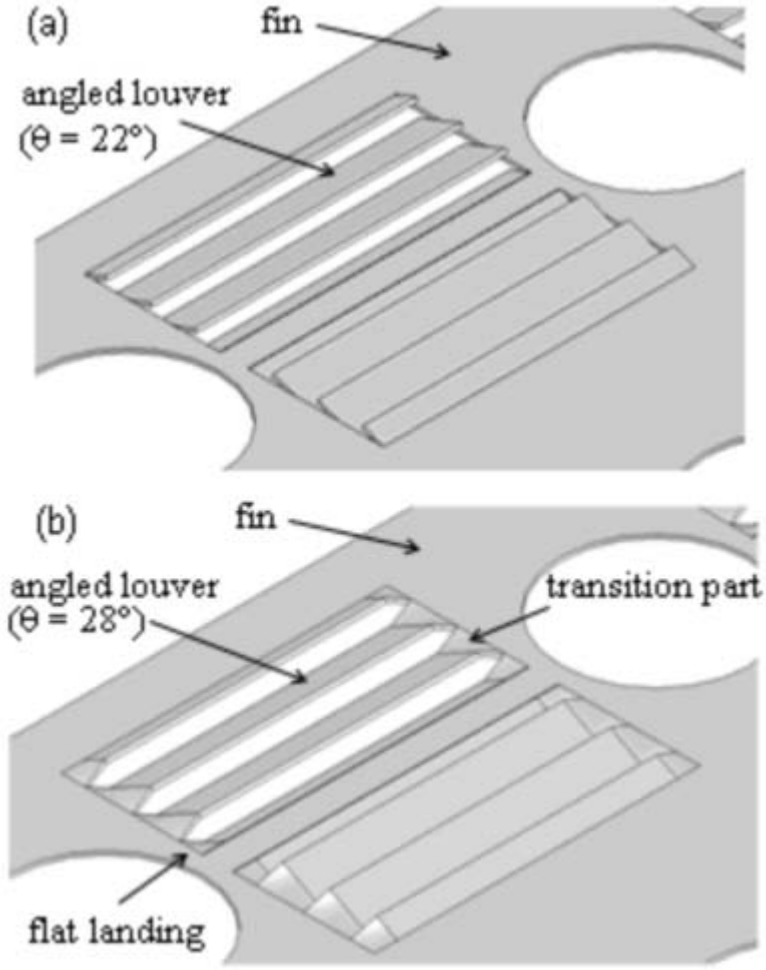
(a)
fin
angled louver
(θ = 22°)
(b)
fin
angled louver
(θ = 28°)
transition part
flat landing

Figure 5

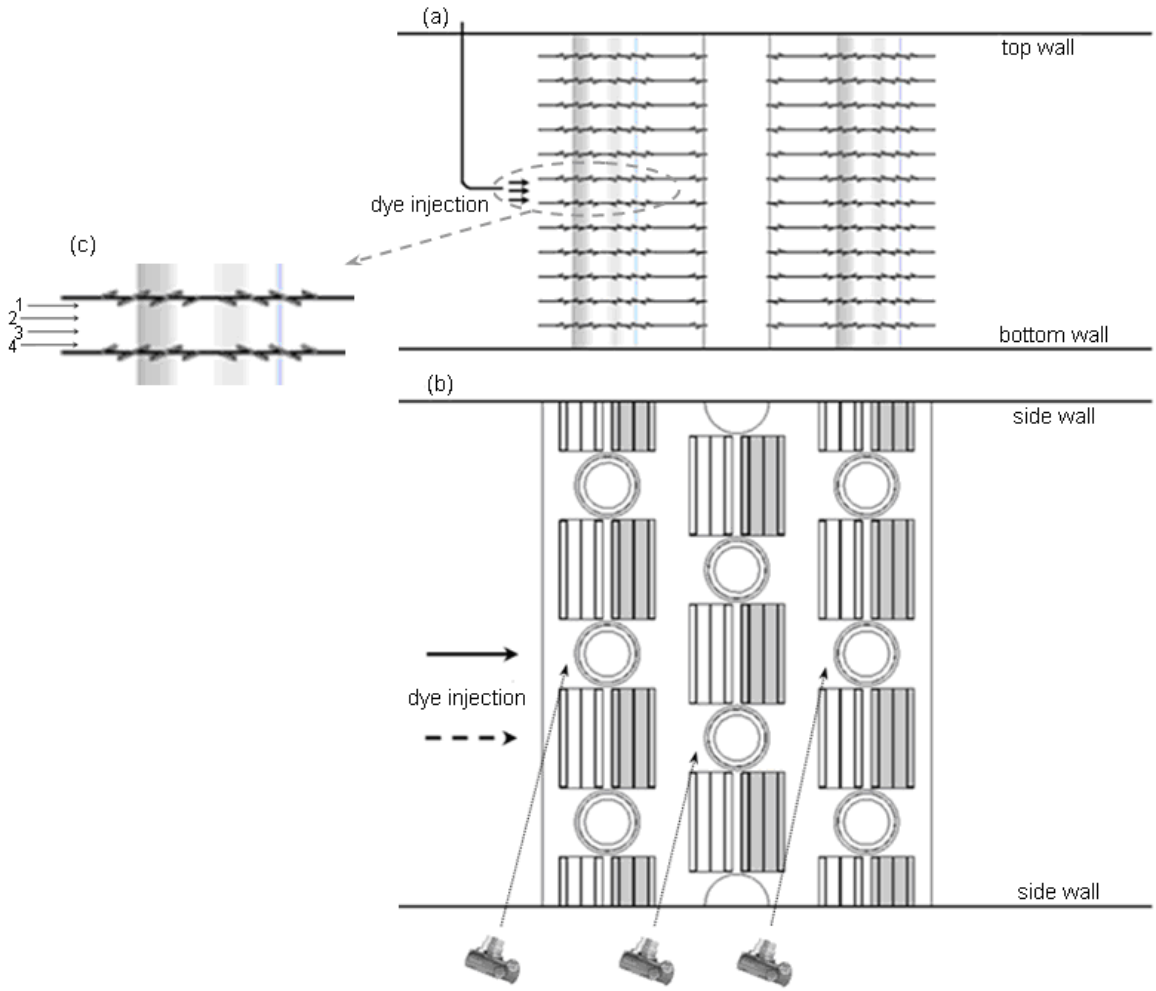
(a)
top wall
dye injection
bottom wall
(c)
1
2
3
4
(b)
side wall
dye injection
side wall

Figure 6

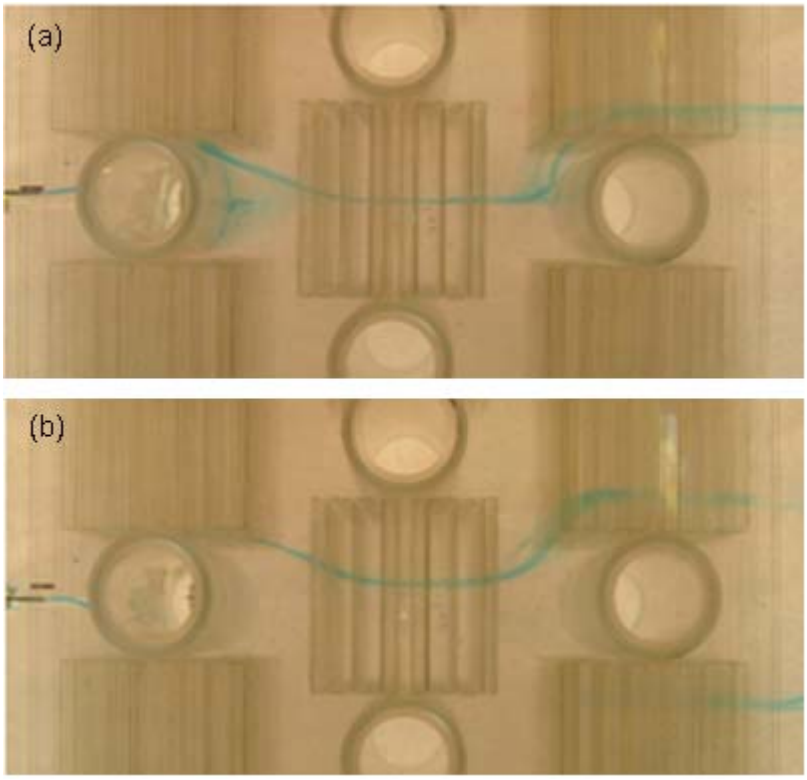

Figure 7

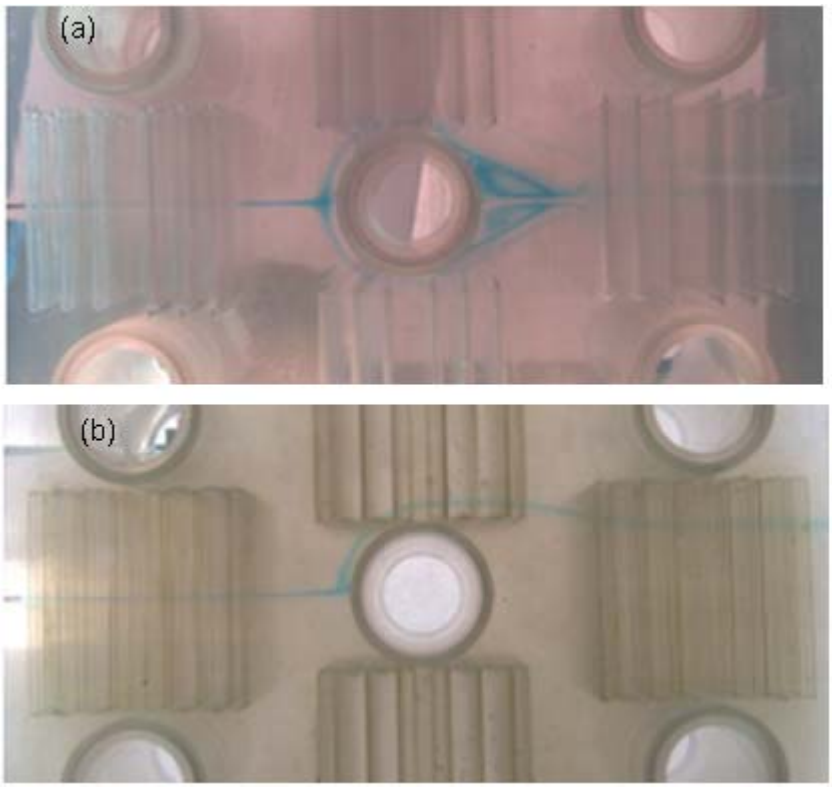

Figure 8

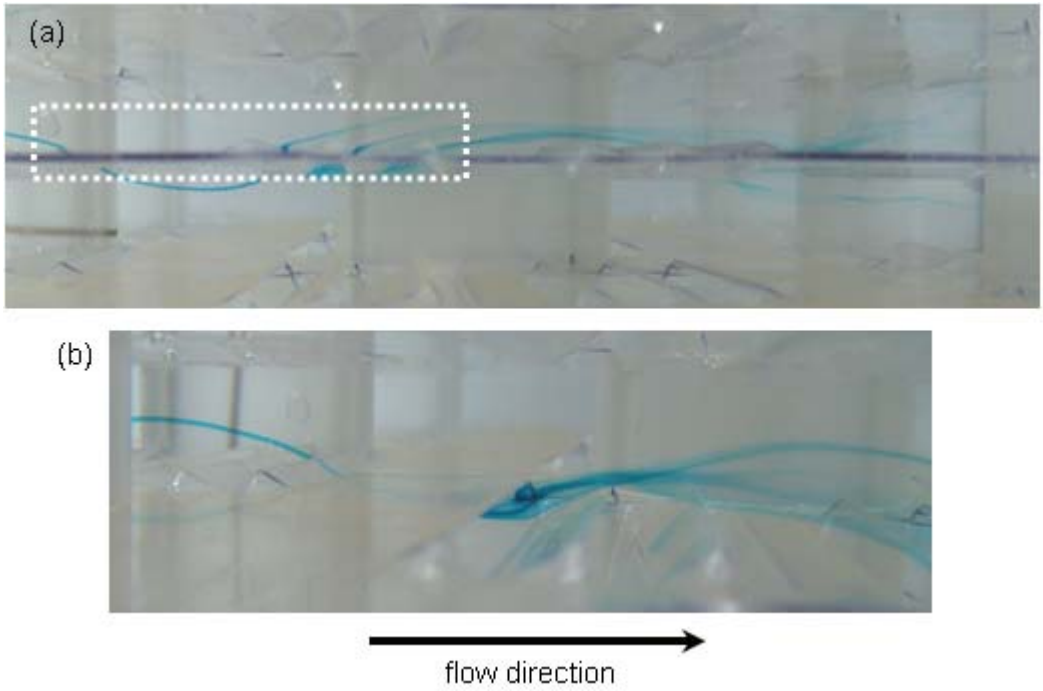

Figure 9

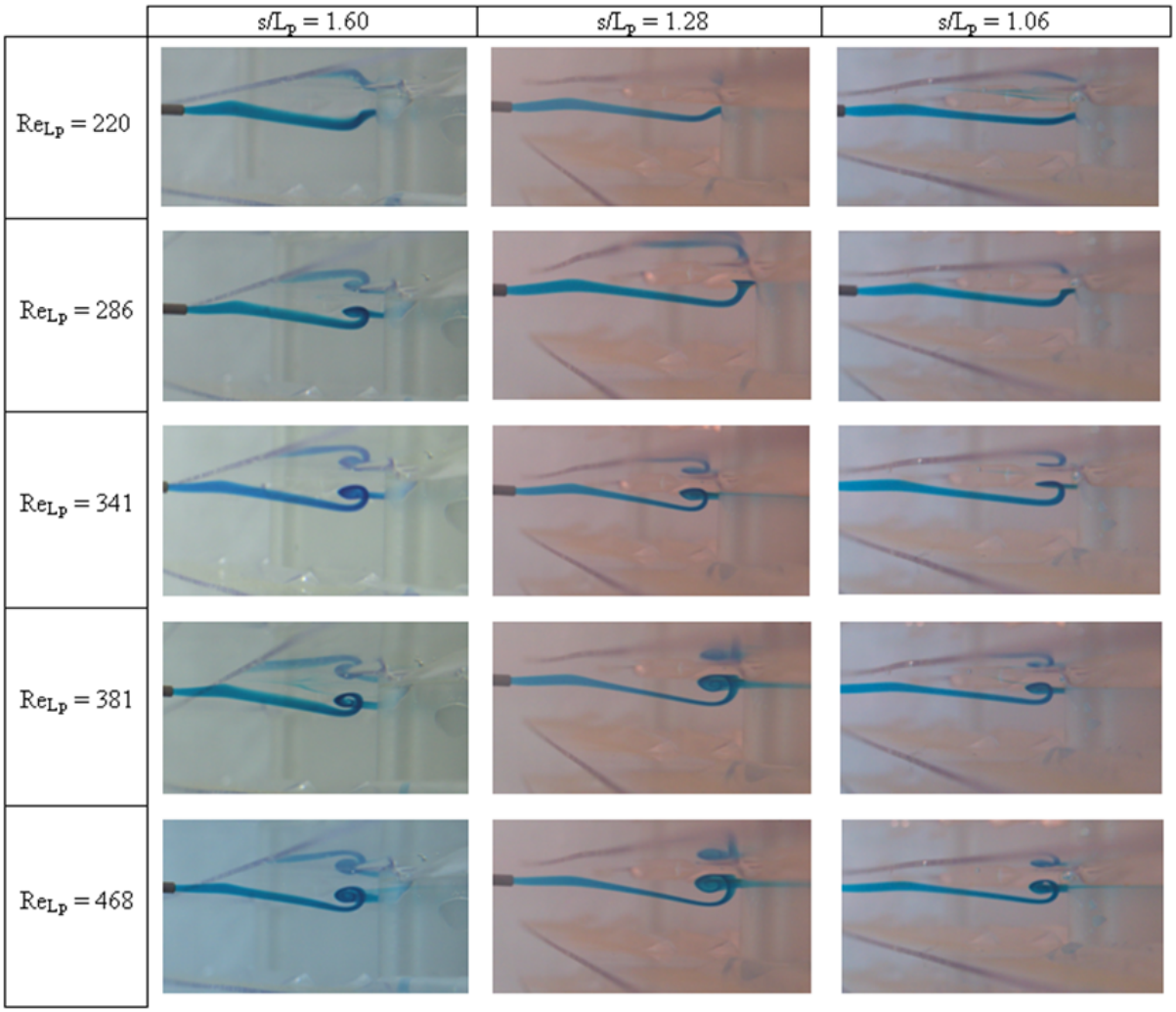
s/Lp = 1.60
s/Lp = 1.28
s/Lp = 1.06
ReLp = 220
ReLp = 286
ReLp = 341
ReLp = 381
ReLp = 468

Figure 10

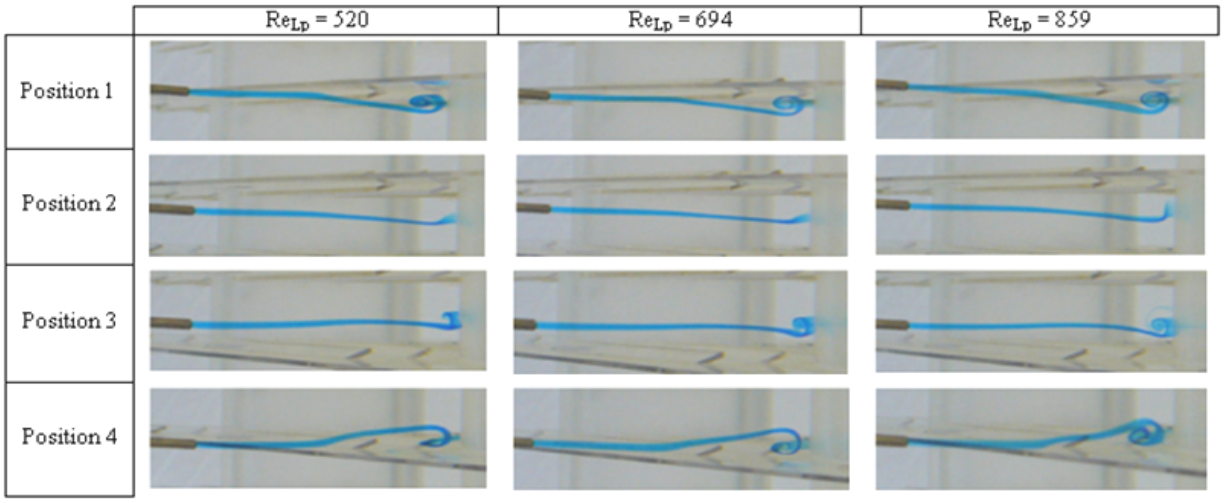
Re_{Lp} = 520
Re_{Lp} = 694
Re_{Lp} = 859
Position 1
Position 2
Position 3
Position 4

Figure 11

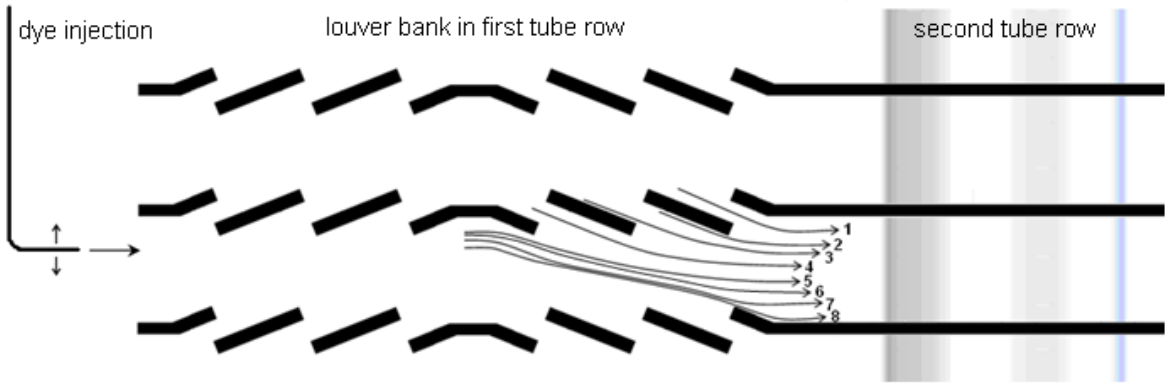
dye injection
louver bank in first tube row
second tube row
1
2
3
4
5
6
7
8

Figure 12

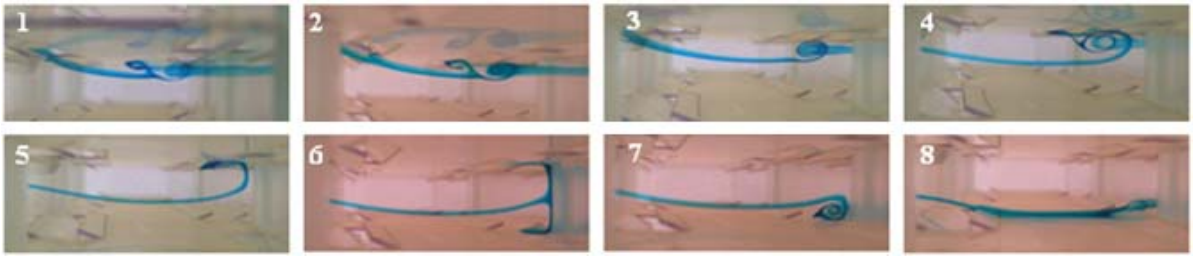

Figure 13

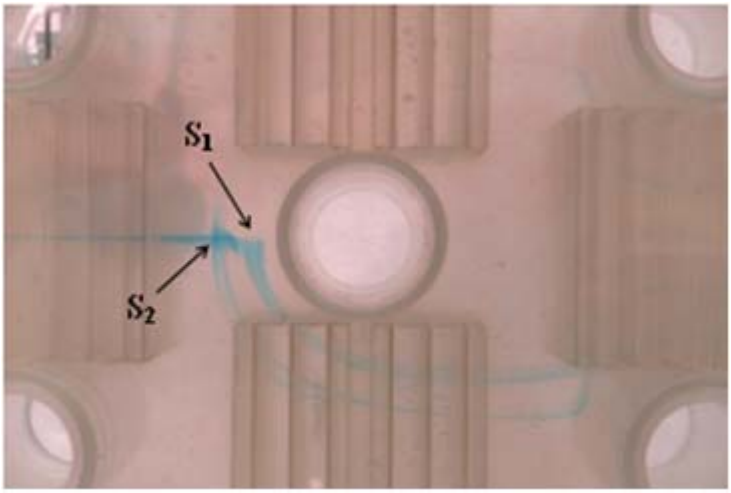

Figure 14

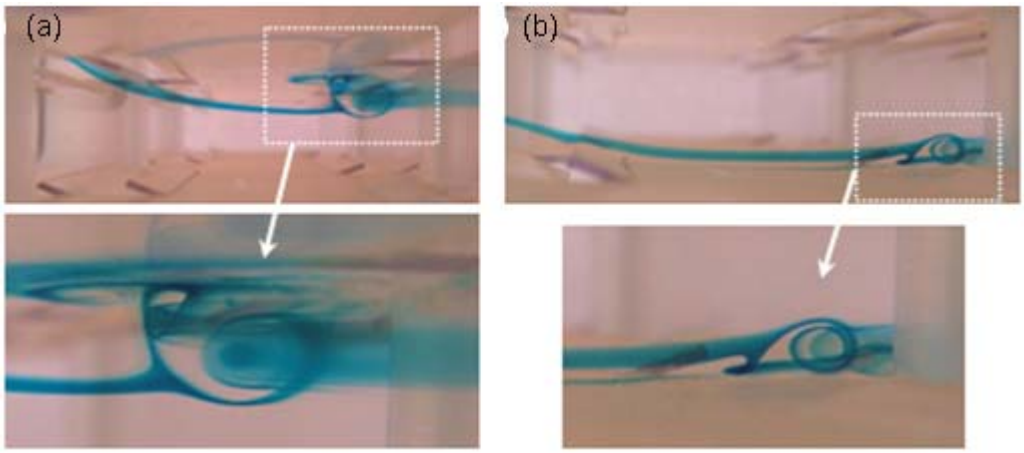

Figure 15

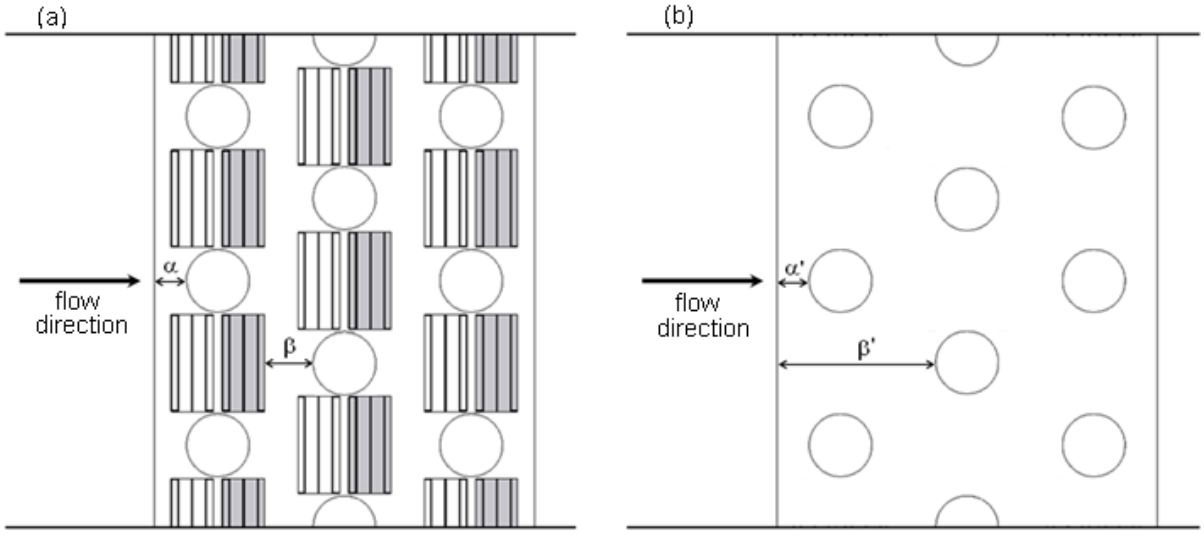

Figure 16

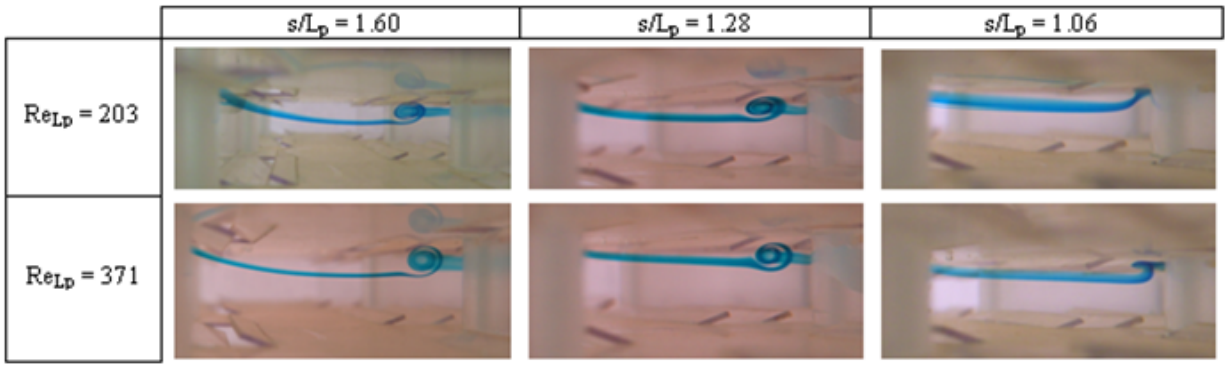

Figure 17